EPJ manuscript No.
(will be inserted by the editor)

Transverse magnetization in Cu/Ni/Cu epitaxial nanorings

Edna C. Corredor[1,2,3] David Coffey[1,3] José I. Arnaudas[2,3] Caroline A. Ross[4] and Miguel Ciria[1,3]

[1] Instituto de Ciencia de Materiales de Aragón, Consejo Superior de Investigaciones Científicas, Zaragoza, Spain.
[2] Instituto Universitario de Nanociencia de Aragón, Universidad de Zaragoza, Zaragoza, Spain.
[3] Departamento de Física de la Materia Condensada, Universidad de Zaragoza, Zaragoza, Spain.
[4] Department of Materials Science and Engineering, Massachusetts Institute of Technology, Cambridge MA USA

Received: date / Revised version: date

Abstract. The micromagnetic structure in epitaxial (001)-oriented Cu/Ni(14 nm)/Cu rings fabricated by electron beam and focused ion beam lithographies with external diameter of 3 μm and linewidths between 100 and 500 nm is presented. We found that a state with radial orientation of the magnetization prevails at remanence. The evaluation of the magnetoelastic, magnetocrystalline and magnetostatic energies shows that a value as low as $1.5 \cdot 10^{-3}$ for the anisotropic relaxation of the in-plane strain components is enough to induce an effective radial easy magnetization direction

PACS. 7 5.30.Gw Magnetic anisotropy – 75.70.Kw Domain structure – 7 5.75.-c Magnetic properties of nanostructures – 6 8.37.Rt Magnetic force microscopy (MFM)

1 Introduction

The strain state in a nanostructured material has become a fine tuning parameter to control physical properties as different as the exciton spectra in semiconductor ZnO microwires [1], the polarization in ferroelectric materials [2], the critical temperature in superconductors [3] or the order temperature in magnetic films [4]. Another fundamental property controlled by the strain state is the magnetic anisotropy through the inverse magnetoelastic (ME) effect: the strain state in the film is coupled to the magnetic lattice and the ME stress coefficients reflect the strength of the spin-orbit coupling. Strain dependence of the magnetic anisotropy energy has been observed in nickel films grown on copper [5–9], and other 3d metal films (Co/Au [10]), and alloys (like $Ni_{90}Fe_{10}$ [11]) as well as in rare earth superlattices [12].

For materials with low magnetization values, which give rise to films with low magnetostatic energy, and cubic crystal structure that results in a feeble magnetocrystalline anisotropy, the contribution of the ME density energy can be particularly important if the residual strain components are of the order of 1% and the ME coupling coefficient is, at least, in the range of MPa. This scenario is found for Ni grown epitaxially on the (001) direction on top of Cu with a tetragonal distortion of the cubic lattice: the in-plane strain is isotropic (ε_{xx}=ε_{yy}= $\varepsilon_{\parallel}$) and the out of the plain strain proportional to the in-plane values: (ε_{zz}=$\varepsilon_{\perp} = -(2c_{12}/c_{11})\varepsilon_{\parallel}$), and all of them are around 1% for Ni films as thick as 10 nm [13]. The total anisotropy energy includes the ME term $e_{ME} = -B_1(\epsilon_{\parallel} - \epsilon_{\perp})cos^2\theta$ with B_1 being a bulk ME coefficient and θ the angle between the film normal [001] (crystallographic direction) and the magnetization vector.

A further step is the control of the magnetic anisotropy and domain configurations in magnetic elements with submicron lateral dimensions, as that is the scale for actual spintronic devices. Planar nanowires and nanorings have been investigated because of their potential use in domain-wall devices proposed for data storage [14] and logic applications [15]. Most reported work has been focused on elements with polycrystalline crystal structure, whose properties are dominated by shape anisotropy. The ring geometry presents two different stable states, usually called vortex and onion states, which can be easily reached by applying a magnetic field in the film plane [16]. Depending on the element dimension, the domain wall (DW) configuration are 180^o transverse or vortex-like DWs [17]. However, materials with different domain states and DW geometries could offer advantages in spintronic applications, as is the case of metallic planar NWs with perpendicular magnetic anisotropy which exhibit enhanced spin-torque efficiency and higher thermal stability compared to those of NWs with in-plane anisotropy [18,19]. Therefore, developing methods for tuning the magnetic anisotropy in nanomagnets may offer new opportunities for spintronic devices.

In this paper we report the fabrication and observation of magnetic domain configurations that defy the magnetostatic anisotropy in magnetic nanorings made in epitaxial Cu/Ni/Cu films with a nickel film thickness t_{Ni} in the range where the effective perpendicular anisotropy coefficient is ≈ 0 and magnetic configurations associated with competing in-plane magnetic anisotropies are expected.

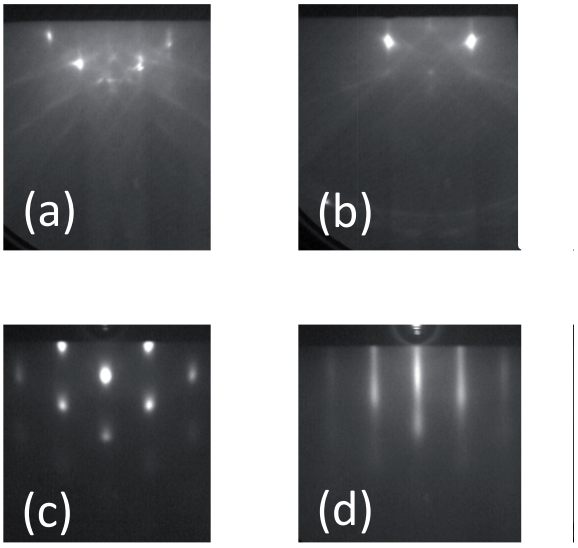

Fig. 1. RHEED patterns obtained for the silicon with the electron beam along the (a) [100] and (b) [110] directions, and for the copper buffer layer along the [110] direction before (c) and after (d) the annealing process.

These rings were fabricated by subtractive processing of epitaxial Cu/Ni/Cu film using focused ion beam and electron beam lithographies combined with dry etching using a metallic hard mask.

2 Experimental details

2.1 Thin film growth

An epitaxial Cu(5nm) / Ni(14nm) / Cu(100nm) film was grown on a Si(001) wafer in a molecular beam epitaxy chamber by electron beam evaporation, using a procedure described elsewhere [13]. The base pressure was 2×10^{-10} Torr and the deposition pressures better than 1×10^{-8} Torr. The native oxide of the Si was eliminated by etching the sample in a HF 10% solution for 30 seconds, rising in DI water and flushing with high purity N_2 before introducing the wafer into the load-lock chamber. This procedure forms a hydrogen-terminated silicon surface and prevents oxidation. Within the evaporation chamber the Si substrate was heated to 400 ^{o} C for several hours and cooled to room temperature, prior to the e-beam evaporation of Cu. Reflection high energy electron diffraction (RHEED) images show spotty features with Kikuchi lines and confirm (1 × 1) surface reconstruction, see Figures 1a and b.

The copper and nickel deposition rates were, respectively, ≈ 0.5 Å/s and 0.3 Å/s, being measured *in-situ* with a quartz crystal calibrated by grazing angle X-ray reflectivity. RHEED reveals the growth in the (001) orientation of the Cu and Ni layers with the following in-plane epitaxial relationships between silicon, copper and nickel layers: Si[110] ‖Cu[100] ‖Ni[100].

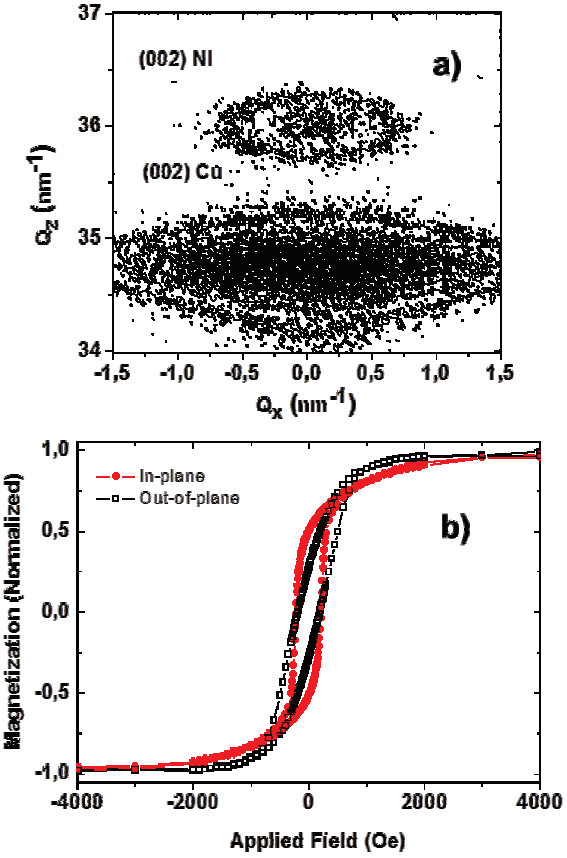

Fig. 2. (Color online) (a) Reciprocal space map in the vicinity of the symmetrical nickel and copper (002) reflection. (b) Hysteresis loops with H perpendicular to the the plane and in-plane for the Cu/Ni/Cu film.

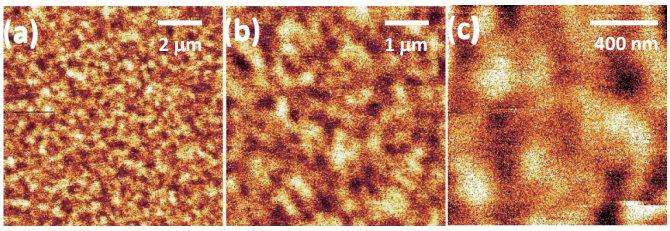

Fig. 3. (Color online) Magnetic force microscopy images of the unpatterned film.

The observed RHEED pattern for the Cu buffer layer consists of sharp points that indicate a 3-dimensional diffraction. This rough surface can be smoothed considerably by a low temperature annealing to about 150^o C for 20 min because lateral diffusion kinetics is greatly enhanced [20]. This procedure is controlled *in situ* by monitoring the RHEED pattens along crystallographic directions. Figures 1c and d show patterns taken with the e-beam along <110> direction before and after the annealing process. Increasing the annealing temperature further caused the complete alloying of the Cu layer with Si.

The thickness of the buffer layer, 100 nm, is chosen in such a way that the lattice parameter of the Cu buffer layer reaches the bulk value, see Figure 2a. The selected nickel film thickness is in the range where the net magnetic anisotropy undergoes reorientation and the easy direction for the magnetization is moving from out of the plane to the in-plane directions as t_{Ni} increases. In this range of thicknesses the ME stress contribution is compensated by the magnetostatic term. For the Ni film studied here, $\varepsilon_\perp$ is about 0.96%, as can be calculated from the reciprocal space map taken around the (002) reflection, see Figure 2a. Therefore $B_1(\epsilon_\parallel - \epsilon_\perp) \approx 0.12$ MJ/m^3, while $(1/2)\mu_0 M^2 \approx 0.14$ MJ/m^3, with M the nickel saturation magnetization. This fact is also observed in the minor differences between the in-plane and out of the plane M-H loops measured by Vibrating Sample Magnetometry (VSM), see Figure 2b. The domain structure (see Figure 3), measured by means of Magnetic Force Microscopy (MFM), shows domains with typical lateral dimension of $\approx$ 200 nm, in accordance with previous work[21].

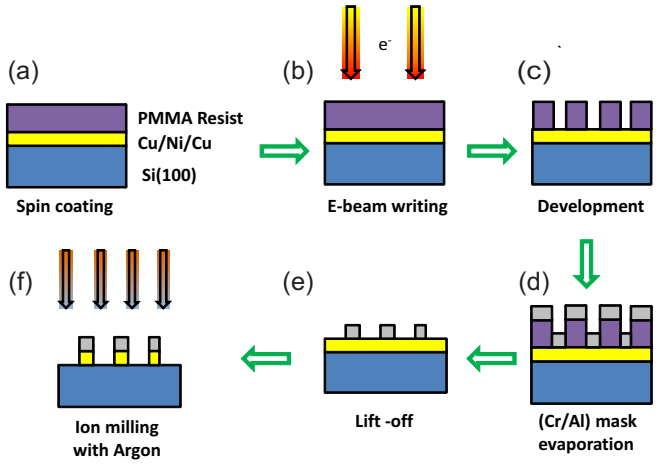

Fig. 4. (Color online) Schematic representation of the patterning of Cu/Ni/Cu/Si films by a subtractive process using electron beam lithography and lift-off techniques.

2.2 Electron beam lithography

Because the elimination of the native oxide would damage a mask prepared directly on the substrate, patterned ring structures have to be fabricated by a subtractive process. The first procedure used in this work includes electron beam (e-beam) lithography, e-beam evaporation of a hard mask, lift-off techniques and ion beam etching. A schematic representation of the patterned process is shown in Figure 4. The Cu/Ni/Cu thin films were coated with a double layer, 120 and 270 nm, of polymethylmethacrylate (PMMA) resin with molecular weights, 50 kg/mol and 950 kg/mol, respectively, baked separately for 10 minutes at 120^{o}C. Exposures were performed at 10 kV accelerating voltage using a beam current of $\approx$ 80 pA such that the delivered dose was 99 $\mu C/cm^2$. The exposed sample was developed with AR 600-56 developer for 30 s with a soft agitation followed by a quench in isopropyl alcohol for 30 seconds, both steps at room temperature. Figure 5a shows a SEM picture of a ring at this point in the process.

After the development, in order to improve the sharpness of the rings and to protect the Ni layer during the ion beam etching step, a Cr(5nm)/Al(14nm) hard mask was evaporated. The bottom Cr block favors adhesion for the high sputtering yield layer of Al. Ion beam etching using Ar ions removes the Ni layer outside the hard mask. The Ar pressure was 4×10^{-4} mbar and the milling rate about 10 nm/min. Processing the sample for 2 minutes produces structures like the ring shown in Fig 5b.

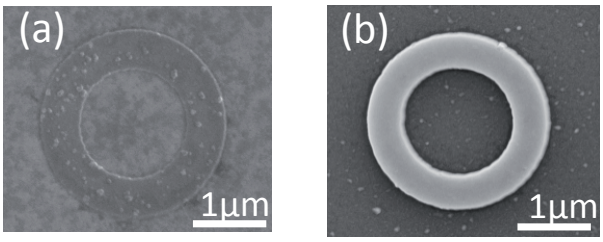

Fig. 5. Scanning electron microscopy taken on a ring after (a)the liftoff and (b) ion beam etching steps.

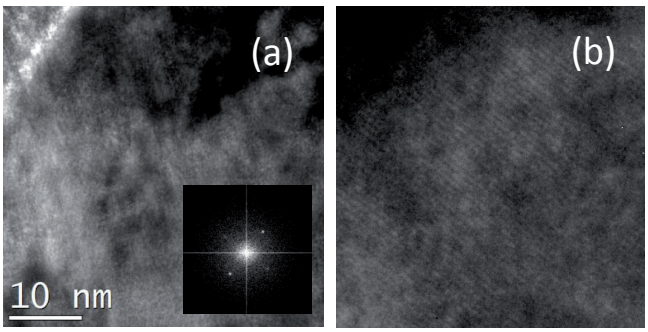

Fig. 6. (a) Transmission electron microscopy image of a ring fabricated by the FIB process, inset FFT of the main image (b) Detailed area of image *a* showing lattice contrast.

2.3 Focused ion beam lithography

A second procedure to fabricate rings can be achieved by means of a focused ion beam facility. This technique uses Ga ion beams to remove the desired film area leaving untouched areas with specific geometry. Using low intensity flux (10 pA at 30 kV) several 3 μm diameter rings were fabricated. The quality of the crystal structure after the patterning process was studied by Transmission Electron Microscopy. Figure 6 displays images of the Cu/Ni/Cu area with electron beam along the [200] Cu direction and the Fast Fourier Transform showing a (200) zone axis. Therefore we conclude that the microfabrication process did not destroy the crystallinity of the epitaxial structure.

3 Experiment

The magnetic domain structure was measured by means of Magnetic Force Microscopy using the tapping technique. Low moment magnetic tips were used to obtain the images shown in Figure 7, taken at zero field after applying magnetic field in the film plane on a ring with an outer diameter D of 3 μm and linewidth W of 250 nm. This image is characteristic of similar images observed for rings with the same diameter and linewidths from 100 nm to 400 nm fabricated by the two procedures described previously. Two main features are observed: first, that the magnetic contrast extends over distances exceeding the ring dimensions and, secondly, that along the radial direction it oscillates between two extreme values at positions around the edges of the ring and passes through zero at approximately the ring mean radius. This stray field is compatible with a transverse structure with the magnetization pointing along radial direction. A simple model supports the qualitative analysis of the MFM images: Figure 8 shows the calculation of the strength of the z component of the fringing field perpendicular to the plane H_z as function of y, the distance from the center of an infinite planar nanowire with uniform magnetization transverse to the wire axis [22], compared with H_z for the same wire with two domains with perpendicular, uniform $\mathbf{M}$ and negligible domain wall thickness. For both cases the stray field is zero at the center of the nanowire although the extreme values are located closer to the edges for the wire with $\mathbf{M}$ in the plane than for the wire with perpendicular domains. For the latter case, it is also noted that $H_z \approx 0$ away of the wire area while H_z decreases more slowly if $\mathbf{M}$ is in the plane, as is observed in the MFM image.

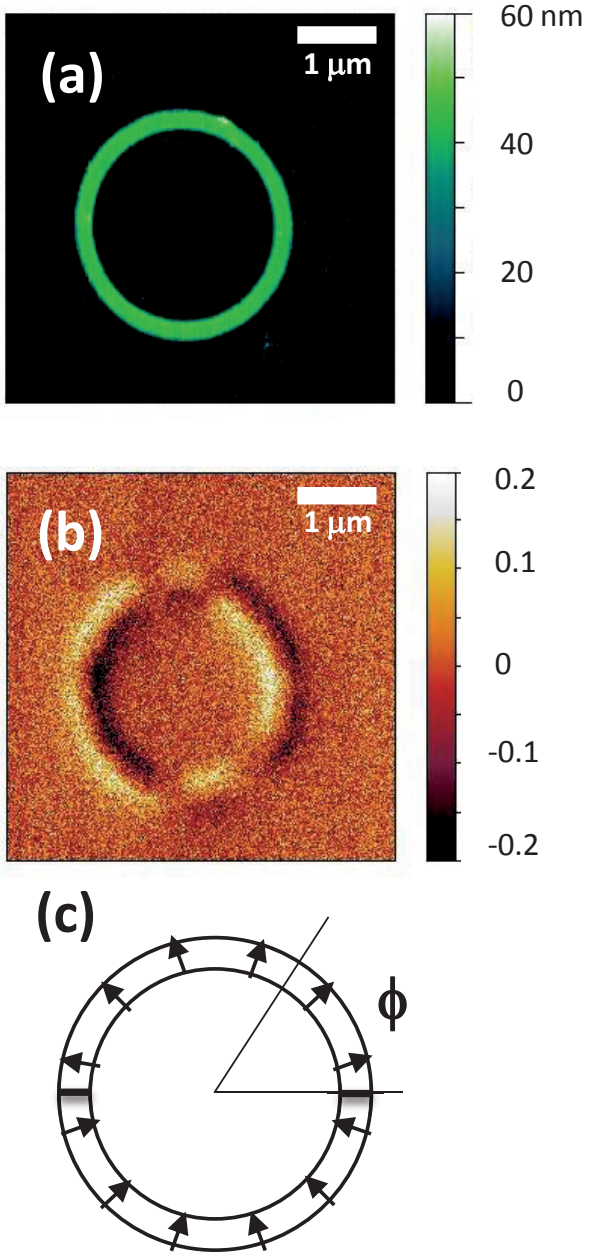

Fig. 7. (Color online) (a)Atomic force microscopy and (b) magnetic force microscopy images taken on a ring with D = 3 μm and W = 250 nm. (c) Sketch of the magnetization in a ring with two domains and $\mathbf{M}$ oriented radially.

4 Analysis

To elucidate the orientation of $\mathbf{M}$ we consider the energy contributions that play a role in the energy balance between the states with $\mathbf{M}$ lying along the radius or circumferentially. We analyze the magnetoelastic, the magnetostatic and the magnetocrystalline contributions to the total density energy as a function of the azimuthal angle ϕ and calculate the difference in energy between the state with $\mathbf{M}$ along the radial direction minus the state with $\mathbf{M}$ tangential to the ring $\Delta e_{anis}(\phi)$. The ring would exhibit magnetization along the radial direction if $\Delta e_{anis}(\phi) < 0$.

4.1 Magnetoelastic Energy

Previous works [23,24] suggest the important role of the ME energy in determining the magnetic configuration in nanowires because of the presence of residual strain in the wires. We note that for Cu/Ni/Cu nanowires the sign of the anisotropic strain relaxation in combination with the sign of the ME stress coefficients favor a transverse ME anisotropy [23]. Here we analyze the ME contribution for a ring with a linewidth of 250 nm assuming an averaged in-plane anisotropic strain value comparable to that measured for an array of nanowires with similar film thickness and wire linewidth.

The general theory for the ME effects [25,26] expresses the ME density of energy e_{mel} of the undistorted crystal as a series of products of tensor strain components and polynomials of the direction cosines of the magnetization related to the coordinate axes. For the Cartesian coordinate system e_{mel} can be written as:

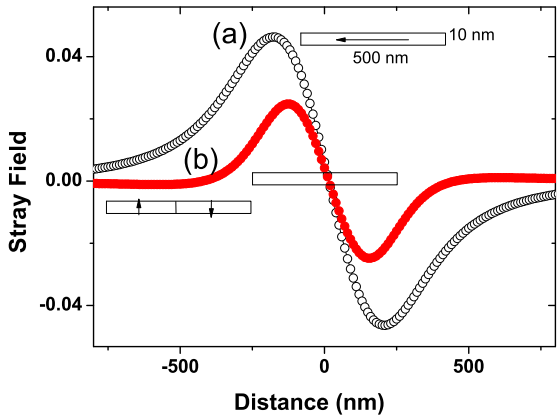

Fig. 8. (Color online) Vertical component H_z of the stray field at z = 225 nm as a function of the distance y transverse to the axis of an infinite rectangular wire with (a) uniform magnetization confined in the plane perpendicular to the wire axis and (b) two domains with **M** perpendicular to the plane. The wire is 500 nm wide and 10 nm thick.

$$e_{mel} = B^{\gamma,2}\left[\left(\alpha_z^2-\frac{1}{3}\right)\left(\epsilon_{zz}-\frac{\epsilon_{xx}+\epsilon_{yy}}{2}\right) + \frac{1}{2}\left(\alpha_x^2-\alpha_y^2\right)\left(\epsilon_{xx}-\epsilon_{yy}\right)\right] + 2B^{\epsilon,2}\left(\alpha_x\alpha_y\epsilon_{xy}+\alpha_y\alpha_z\epsilon_{yz}+\alpha_z\alpha_x\epsilon_{zx}\right) \quad (1)$$

The number of independent first-order ME coefficients is reduced to two ($B^{\gamma,2}$ and $B^{\epsilon,2}$ that correspond to the usual B_1 and B_2 ME coefficients [22]). From equation (4.1) it can be deduced that different lattice deformations produce different magnetization states that are governed by the same ME coefficient. Thus, for the γ-terms, inside the square bracket, the strain polynomial multiplying $\alpha_z^2-1/3$ corresponds to a tetragonal distortion $(a,a,a)\rightarrow(c,a',a')$ that may introduce a perpendicular anisotropy, while the second strain term, which is multiplied by $\alpha_x^2-\alpha_y^2$, describe the contribution due to the breaking of the in-plane symmetry $(a,a)\rightarrow(a',b')$. The last contribution is fundamental in nanowires since the isotropic in-plane strain is broken by the patterning process.

It is more appropriate to describe the problem in the cylindrical coordinate system because it reflects the symmetry of the ring. The strain tensor components in the cylindrical reference basis can be obtained by performing the tensorial transformation for 2nd order tensors: $\epsilon_{ij} = a_{ik}\epsilon_{kl}a_{lj}$ where the subscripts stand for the tensor coordinates; i, j are assigned to Cartesian components (x, y, z) and k,l to the cylindrical system (r, ϕ, z). The a's correspond to the transformation tensor: $a_{11} = a_{22} = cos\phi$, $a_{12} = -sin\phi$, $a_{21} = sin\phi$, $a_{33} = 1$, $a_{13} = a_{31} = a_{23} = a_{32} = 0$, therefore:

$$\begin{aligned}
\epsilon_{xx} &= \epsilon_{rr}cos^2\phi + \epsilon_{\phi\phi}sin^2\phi - \epsilon_{r\phi}sin2\phi\\
\epsilon_{yy} &= \epsilon_{rr}sin^2\phi + \epsilon_{\phi\phi}cos^2\phi + \epsilon_{r\phi}sin2\phi\\
\epsilon_{zz} &= \epsilon_{zz}\\
\epsilon_{xy} &= \left(\epsilon_{rr}-\epsilon_{\phi\phi}\right)sin\phi cos\phi + \epsilon_{r\phi}\left(cos^2\phi - cos^2\phi\right)\\
\epsilon_{yz} &= \epsilon_{rz}cos\phi - \epsilon_{\phi z}sin\phi\\
\epsilon_{zx} &= \epsilon_{rz}sin\phi + \epsilon_{\phi z}cos\phi
\end{aligned} \quad (2)$$

and for the cosines of the magnetization:

$$\begin{aligned}
\alpha_x &= \alpha_r cos\phi - \alpha_\phi sin\phi\\
\alpha_y &= \alpha_r sin\phi + \alpha_\phi cos\phi\\
\alpha_z &= \alpha_z
\end{aligned} \quad (3)$$

obtaining for e_{mel}

$$\begin{aligned}
e_{mel} = B_1\Bigg\{&\left(\alpha_z^2-\frac{1}{3}\right)\left(\epsilon_{zz}-\frac{\epsilon_{rr}+\epsilon_{\phi\phi}}{2}\right)\\
&+\frac{1}{2}\left[\left(\alpha_r^2-\alpha_\phi^2\right)cos2\phi - 2\alpha_r\alpha_\phi sin2\phi\right]\\
&\times\left[\left(\epsilon_{rr}-\epsilon_{\phi\phi}\right)cos2\phi - 2\epsilon_{r\phi}sin2\phi\right]\Bigg\}\\
&+2B_2\Bigg\{\left[\frac{1}{2}sin2\phi\left(\alpha_r^2-\alpha_\phi^2\right)+cos^2\phi\alpha_r\alpha_\phi\right]\\
&\times\left[\frac{1}{2}\left(\epsilon_{rr}-\epsilon_{\phi\phi}\right)sin2\phi + \epsilon_{r\phi}cos2\phi\right]\\
&+\epsilon_{rz}\left[\alpha_r sin2\phi + \alpha_\phi cos2\phi\right]\alpha_z\\
&+\epsilon_{\phi z}\left[\alpha_r cos2\phi - \alpha_\phi sin2\phi\right]\alpha_z\Bigg\}
\end{aligned} \quad (4)$$

Therefore the difference in e_{mel} if **M** is aligned along the radius (α_r=1, α_ϕ=0) and tangent to the ring (α_r=0, α_ϕ=1) is:

$$\Delta e_{mel} = \left(B_1 cos^2 2\phi + B_2 sin^2 2\phi\right)\left(\epsilon_{rr}-\epsilon_{\phi\phi}\right) \quad (5)$$

The magnitude of this contribution depends on the existence of an inequality between the radial ϵ_{rr} and the tangential strain $\epsilon_{\phi\phi}$. Notice that we have assumed that the shear strains are negligible. The presence of a combination of the two ME stresses multiplying the strain polynomial in equation (5) complicates the variation of the sign of this contribution with ϕ. This function oscillates between the values of B_1 and B_2 every $\pi/2$ and, thus, if the sign of the $B's$ is different, the sign of the ME contribution to Δe_{mel} would oscillate with ϕ. For nickel both B_1 and B_2 are positive.

The anisotropy of the relaxation of the in-plane strain components in nanowires with t_{Ni} = 10 nm and width of 200 nm has been measured by X-ray diffraction [23], providing a value of $\approx 3.4{\cdot}10^{-3}$. This value is obtained as the difference between the strain along the wire axis minus the stain transverse to the wire axis. For a ring, those strains can be associated, respectively, to $\epsilon_{\phi\phi}$ and ϵ_{rr}, thus $\epsilon_{rr}-\epsilon_{\phi\phi} < 0$ and $\Delta e_{mel} < 0$ for any value of ϕ, see Figure 9, favoring the radial orientation of **M**. Note that the sign of $\epsilon_{rr}-\epsilon_{\phi\phi}$ is related to the sign of the in

plane film strain, that is positive for the Ni/Cu system because the Ni undergoes a tensile stress, and therefore to the sign of the misfit between film and substrate lattice parameters.

4.2 Magnetostatic Energy

The magnetostatic energy e_{ms} is calculated evaluating the magnetostatic potential, a process used elsewhere to obtain e_{ms} for a ring with the onion configuration [27]. For the sake of simplicity we consider the case of a ring with two radial domains, see sketch in Figure 7c, and negligible domain width; thus the tangential component of $\mathbf{M}(\mathbf{r})$ is zero and $\mathbf{M}(\mathbf{r})= M_r(\phi)\hat{r}$, with $M_r = M$ for $0 > \phi > \pi$ and $M_r = -M$ for $\pi > \phi > 2\pi$.

The radial configuration of $\mathbf{M}$ generates surface $(\mathbf{M}\cdot\widehat{n})$ and volumetric $(\text{-}\nabla \cdot \mathbf{M})$ magnetic charges, resulting in volume $e_{ms,v}$ and surface $e_{ms,s}$ contributions to e_{ms} with the following expressions:

$$e_{ms,v} = \frac{1}{2}\mu_0 M^2 \frac{1}{\pi(1-\beta^2)\gamma}\sum_{p=1}^{\infty}\frac{Q_v}{p^2} \tag{6}$$

$$e_{ms,s} = \frac{1}{2}\mu_0 M^2 \frac{1}{\pi(1-\beta^2)\gamma}\sum_{p=1}^{\infty}\frac{Q_s}{p^2} \tag{7}$$

with

$$Q_{v,p}(\beta,\gamma) = \frac{8}{\pi}\int_{\beta}^{1} dw \int_{\beta}^{1} xdx \int_{0}^{\infty} [J_{p-1}(xy) - J_{p+1}(xy)] \times \frac{e^{-\gamma y} + \gamma y - 1}{y} J_p(wy) \tag{8}$$

$$Q_{s,p}(\beta,\gamma) = \frac{8}{\pi}\int_{\beta}^{1} xdx \int_{0}^{\infty} [J_p(y) - \beta J_p(\beta y)] \times \frac{e^{-\gamma y} + \gamma y - 1}{y} [J_{p-1}(xy) - J_{p+1}(xy)] \tag{9}$$

here, $\beta = 1-(2W/D)$ and $\gamma = 2t_{ni}/D$; J_p are Bessel functions of the first kind that appear because of the cylindrical symmetry of the ring geometry. The sums in equations (6) and (7) run over positive and odd values of p due to the symmetry of the domain configuration. The factor p^{-2} arises from the integration of $\mathbf{M}$ over the angular variable ϕ. $Q_{v,p}$ and $Q_{s,p}$ have been evaluated and, because of the presence of the factor p^{-2}, considering only a few terms in equations (6) and (7) is sufficient to obtain a reasonable value for the density of magnetostatic energy. For the ring considered here, $e_{ms} \approx 10$ kJ/m^3.

There are no magnetic poles for a vortex state (α_r=0, α_ϕ=1) and the magnetostatic energy is zero, therefore Δe_{ms} takes the value of 10 kJ/m^3.

4.3 Magnetocrystalline Energy

The magnetocrystalline anisotropy for cubic crystals for the lowest order is expressed as: $e_{mc} = K_1(\alpha_x{}^2\alpha_y{}^2 + \alpha_y{}^2\alpha_z{}^2 + \alpha_z{}^2\alpha_x{}^2)$, becoming:

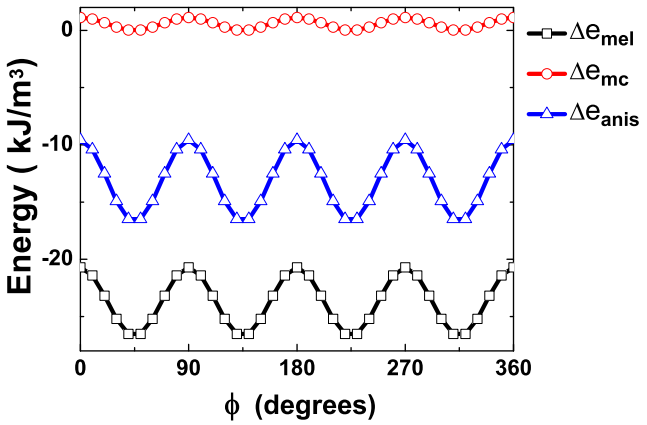

Fig. 9. (Color online) Angular dependence of $\Delta e_{anis}(\phi)$ for a ring with 3 μm diameter, ω= 250 nm width, and $\epsilon_{rr} - \epsilon_{\phi\phi} \approx$ -0.003. $\Delta e(\phi)_{mel}$, $\Delta e(\phi)_{mc}$ are also shown

$$e_{mc} = K_1\left[(\alpha_r cos\phi - \alpha_\phi sin\phi)^2(\alpha_r sin\phi + \alpha_\phi cos\phi)^2\right], \tag{10}$$

in cylindrical coordinates, using equations (3). From the point of view of the magnetocrystalline energy, there is a cost of keeping $\mathbf{M}$ along the radial direction that depends on ϕ and can be evaluated by putting α_r=1, α_ϕ=0 in equation (10).

$$\Delta e_{mc} = \frac{1}{4}K_1\left[1 - sin^2 2\phi\right] \tag{11}$$

Notice that this cost is zero for $\phi = \pi/4$ and maximum $(K_1/4)$ for $\phi = 0$.

4.4 Discussion

The energy balance $\Delta e_{anis}(\phi)$ for a ring with $\omega = 250$ nm and an averaged $(\epsilon_{rr} - \epsilon_{\phi\phi})$ of -0.003, a value in the range of the experimental data measured for wires with similar width and Ni thickness, is displayed in Figure 9, taking B_1 = 6.9 MPa, B_2 = 8.9 MPa [28] and $K_1 = -4.5\times10^3 J/m^3$. $\Delta e_{anis}(\phi)$ is negative independently of ϕ, meaning that the radial orientation of $\mathbf{M}$ is favored over the tangential direction for the complete ring. It can be observed that $\Delta e_{mel}(\phi)$ is the largest contribution to $\Delta e_{anis}(\phi)$. The calculations show that $\Delta e_{anis}(\phi)$ is kept at negative values even if $(\epsilon_{rr} - \epsilon_{\phi\phi})$ decreases to values as low as -1.5 $\times10^3$. Therefore the radial orientation of $\mathbf{M}$ observed in epitaxial rings can be attributed to the ME contribution.

This work shows the relevance of the ME interaction in the control of the magnetic state in nanomagnets. For example, magnetic circuits made on epitaxial layers will include nanowires with the axes along different crystallographic directions, connected with circular segments. The orientation of the magnetization of those elements can be chosen through the election of the sign for the ME stress

coefficients. Thus, materials with different sign of B offer the possibility of combining elements with these transverse magnetic orientations with the usual longitudinal orientation of M, enabling new configurations of domain walls to be created.

5 Summary

Epitaxial rings of Cu/Ni/Cu have been fabricated by e-beam and focused ion beam techniques in the range of thicknesses where the effective magnetic anisotropy in the unpatterned film is ≈ 0. The micromagnetic structure shows an unusual orientation of the magetization along the radial direction of the ring. This effect is explained due to the ME anisotropy generated by an anisotropic relaxation of the epitaxial strain observed in the continuous film.

We acknowledge the use of the microscopy infrastructure available in the Laboratorio de Microscopías Avanzadas (LMA) at Instituto de Nanociencia de Aragón (University of Zaragoza, Spain). This work has been supported by Spanish MICINN (Grants No. MAT2009-10040) and Gobierno de Aragón (Grants E81 and PI049/08) and Fondo Social Europeo.

References

1. Z.M. Liao, H.C. Wu, Q. Fu, X. Fu, X. Zhu, J. Xu, I.V. Shvets, Z. Zhang, W. Guo, Y. Leprince-Wang et al., Sci. Rep. **2**, 452 (2012)
2. X. Marti, I. Fina, V. Skumryev, C. Ferrater, M. Varela, L. Fabrega, F. Sanchez, J. Fontcuberta, Appl. Phys. Lett. **95**, 142903 (3) (2009)
3. S. Trommler, R. Hühne, K. Iida, P. Pahlke, S. Haindl, L. Schultz, B. Holzapfel, New J. Phys. **12**, 103030 (2010)
4. R.S. Beach, J.A. Borchers, A. Matheny, R.W. Erwin, M.B. Salamon, B. Everitt, K. Pettit, J.J. Rhyne, C.P. Flynn, Phys. Rev. Lett. **70**, 3502 (1993)
5. R. Jungblut, M.T. Johnson, J. aan de Stegge, A. Reinders, F.J.A. den Broeder, J. Appl. Phys. **75**, 6424 (1994)
6. B. Schulz, K. Baberschke, Phys. Rev. B **50**, 13467 (1994)
7. F. Huang, M.T. Kief, G.J. Mankey, R.F. Willis, Phys. Rev. B **49**, 3962 (1994)
8. G. Bochi, C.A. Ballentine, H.E. Inglefield, C.V. Thompson, R.C. O'Handley, H.J. Hug, B. Stiefel, A. Moser, H.J. Güntherodt, Phys. Rev. B **52**, 7311 (1995)
9. K. Ha, R.C. O'Handley, J. Appl. Phys. **85**, 5282 (1999)
10. A. Murayama, K. Hyomi, J. Eickmann, C.M. Falco, Phys. Rev. B **60**, 15245 (1999)
11. M. Ciria, K. Ha, D. Bono, R.C. O'Handley, J. Appl. Phys. **91**, 8150 (2002)
12. L. Benito, J.I. Arnaudas, M. Ciria, C. de la Fuente, A. del Moral, R.C.C. Ward, M.R. Wells, Phys. Rev. B **70**, 052403 (2004)
13. K. Ha, M. Ciria, R.C. O'Handley, P.W. Stephens, S. Pagola, Phys. Rev. B **60**, 13780 (1999)
14. S.S.P. Parkin, M. Hayashi, L. Thomas, Science **320**, 190 (2008)
15. D.A. Allwood, G. Xiong, C.C. Faulkner, D. Atkinson, D. Petit, R.P. Cowburn, Science **309**, 1688 (2005)
16. C.A. Ross, F.J. Castaño, D. Morecroft, W. Jung, H.I. Smith, T.A. Moore, T.J. Hayward, J.A.C. Bland, T.J. Bromwich, A.K. Petford-Long, J. Appl. Phys. **99**, 08S501 (6) (2006)
17. M. Kläui, C. Vaz, L. Heyderman, U. Rüdiger, J. Bland, J. Magn. Mag. Mat. **290 − 291**, 61 (2005)
18. D. Ravelosona, D. Lacour, J.A. Katine, B.D. Terris, C. Chappert, Phys. Rev. Lett. **95**, 117203 (2005)
19. S.W. Jung, W. Kim, T.D. Lee, K.J. Lee, H.W. Lee, Appl. Phys. Lett. **92**, 202508 (3) (2008)
20. R.A. Lukaszew, Y. Sheng, C. Uher, R. Clarke, Appl. Phys. Lett. **76**, 724 (2000)
21. S. Hameed, P. Talagala, R. Naik, L.E. Wenger, V.M. Naik, R. Proksch, Phys. Rev. B **64**, 184406 (2001)
22. R.C. O'Handley, *Modern Magnetic Materials: Principles and Applications* (John Wiley Sons, 2000)
23. M. Ciria, F.J. Castaño, J.L. Diez-Ferrer, J.I. Arnaudas, B.G. Ng, R.C. O'Handley, C.A. Ross, Phys. Rev. B **80**, 094417 (2009)
24. D. Navas, C. Nam, D. Velazquez, C.A. Ross, Phys. Rev. B **81**, 224439 (2010)
25. E. Callen, H.B. Callen, Phys. Rev. **139**, A455 (1965)
26. J. Rouchy, E. du Tremolet de Lacheisserie, Z. Physik B **36**, 67 (1979)
27. P. Landeros, J. Escrig, D. Altbir, M. Bahiana, J. dAlbuquerque e Castro, J. Appl. Phys. **100**, 044311 (2006)
28. E.W. Lee, M.A. Asgar, Proc. R. Soc. A **326**, 73 (1971)